Lateral Displacement Estimation Using Tissue Incompressibility

Mark A. Lubinski, *Student Member, IEEE*, Stanislav Y. Emelianov, *Member, IEEE*, K. R. Raghavan, *Member, IEEE*, Andrew E. Yagle, *Member, IEEE*, Andrei R. Skovoroda, and Matthew O'Donnell, *Fellow, IEEE*

Abstract— **Using the incompressibility property of soft tissue, lateral displacements can be reconstructed from axial strain measurements. Results of simulations and experiments on gelatin-based tissue equivalent phantoms are compared with theoretical displacements, as well as estimates derived from traditional speckle tracking. Incompressibility processing greatly improves the accuracy and signal-to-noise ratio (SNR) of lateral displacement measurements compared with more traditional speckle tracking.**

I. Introduction

A NUMBER of quantitative 2-D tracking techniques have been proposed for ultrasonic displacement imaging. They include optical flow [1], 2-D correlation [2], [3], and Fourier-based methods [4]. Although all measure both axial (i.e., along the beam direction) and lateral (i.e., perpendicular to the beam direction) displacements, errors in the two components are not the same. For an ultrasound system, the axial resolution is limited by the system Q and the transducer frequency, whereas the lateral resolution is limited by the beamwidth [5]. Thus, lateral displacement estimates will be many times less accurate than axial [6]. The accuracy of lateral tracking is especially important in elasticity imaging, where, in general, all displacement components and spatial derivatives are needed to reconstruct the elastic modulus [7]. In the Appendix, the variance anisotropy of displacement estimates using correlation methods is analyzed. With a constant f/number (f/num) system, additive white noise, and a high signal-to-noise ratio (SNR), the analysis shows that the variance of lateral displacement estimates should be about 40 (f/num)^2 times worse than that of axial. To overcome this anisotropy, we propose to estimate the lateral displacement using the incompressibility property of soft tissue.

For any mechanical body, the divergence of the displacement vector $\boldsymbol{u}$ is a measure of the volume change due to deformation. Deformation produces no volume change in incompressible materials, hence

$$\nabla \cdot \boldsymbol{u} = 0. \tag{1}$$

Previous studies have shown that soft tissues and tissue-like materials can be well modeled as incompressible [8], [9]. Generally, for compressible media, this condition is valid with an accuracy proportional to $\delta = 0.5 - \nu$, where ν is the Poisson's ratio [10]. If (1) is used for slightly compressible media, the relative error in displacement components will also be proportional to δ [10].

Using (1) for a deformed system, it is possible to reconstruct one of the unknown components of $\boldsymbol{u}$ based on the two others. As an initial test of the approach, we use a simplified deformation, a plane strain state. The methods are general, however, and can be extended for a 3-D strain state [11].

For an object in a plane strain state, the normal strain in the out-of-plane direction is zero [12]. Note that this does not assume that out-of-plane motion is zero, only that it is uniform. This state can be approximated if the deformation of the system is such that the out of plane strain components are negligible compared to the others. For this state, (1) can be reduced to a 2-D problem in the x–y plane

$$\frac{\partial u}{\partial x} + \frac{\partial v}{\partial y} = 0. \tag{2}$$

Here, u is the component of the displacement $\boldsymbol{u}$ in the x–direction and v is the component in the y-direction. This equation holds at every position in the plane.

Arbitrarily letting x be the lateral direction and y the axial direction, (2) can be rewritten in terms of the normal strains

$$\varepsilon_{xx}(x,y) + \varepsilon_{yy}(x,y) = 0, \tag{3}$$

where ε_{yy} is the normal axial component of the second ranked symmetric strain tensor and ε_{xx} is the normal lateral component

$$\varepsilon_{xx}(x,y) = \left.\frac{\partial u}{\partial x}\right|_{(x,y)}, \tag{4a}$$

$$\varepsilon_{yy}(x,y) = \left.\frac{\partial v}{\partial y}\right|_{(x,y)}. \tag{4b}$$

Manuscript received January 23, 1995; revised October 13, 1995. This work was supported in part by NIH Grant DK47324, NSF Grant MIP-8858082, and by a Research Partnership Award from the H. H. Rackham School of Graduate Studies of the University of Michigan. The work of M. A. Lubinski was supported by a GAANN Fellowship from the Department of Education.

M. A. Lubinski and M. O'Donnell are with the Electrical Engineering and Computer Science Department, and the Bioengineering Program, University of Michigan, Ann Arbor, MI 48109 USA (e-mail: odonnel@eecs.umich.edu).

S. Y. Emelianov is with the Electrical Engineering and Computer Science Department, and the Bioengineering Program, University of Michigan, Ann Arbor, MI 48109 USA, and the Institute of Mathematical Problems of Biology, Russian Academy of Sciences, Pushchino, Russia 142292.

K. R. Raghavan and A. E. Yagle are with the Electrical Engineering and Computer Science Department, University of Michigan, Ann Arbor, MI 48109 USA.

A. R. Skovoroda is with the Institute of Mathematical Problems of Biology, Russian Academy of Sciences, Pushchino, Russia 142292.

Publisher Item Identifier S 0885-3010(96)01755-8.

Along any given range y_0, (4a) can be integrated to reconstruct the lateral displacement at that range

$$u(x, y_0) = \int_{x_0}^{x} [\varepsilon_{xx}(x', y_0)]\, dx' + u(x_0, y_0). \tag{5}$$

Using the incompressibility property expressed in (3), the unknown lateral strain can be replaced by the measured axial strain

$$u(x, y_0) = \int_{x_0}^{x} [-\varepsilon_{yy}(x', y_0)]\, dx' + u(x_0, y_0). \tag{6}$$

Hence, the lateral displacement can be reconstructed using measurements of the normal axial strain given the lateral displacement at only one position along each range, $u(x_0, y_0)$.

The continuous differential operator needed to compute the normal axial strain from the axial displacement can be approximated with finite differences. With this approximation, the normal axial strain is proportional to the differential axial displacement (i.e., $\varepsilon_{yy} = \Delta V/\Delta x$). The variance in the differential displacement, ΔV, is not more than two times larger than the axial displacement variance. Considering that the measured lateral displacement variance is about 40 (f/num)^2 times the axial displacement variance (see the Appendix), (6) suggests that more accurate estimates of the lateral displacement can be obtained using incompressibility processing. In the next section, we present a specific method based on (6), and show that it yields more accurate lateral displacement estimates compared to direct approaches such as correlation-based speckle tracking.

II. Incompressibility Processing

In the limit of ideal measurements, lateral displacements estimated from speckle tracking must be equivalent to those estimated by (6). For imperfect measurements, the difference in these two estimates produces an error E

$$E = u(x, y) - u_m(x, y), \tag{7}$$

where $u_m(x, y)$ is the "measured" lateral displacement obtained from speckle tracking and $u(x, y)$ is the lateral displacement predicted by (6). For any given point (x_0, y_0), a total squared error function, Φ, based on (6) and (7) can be defined as

$$\begin{aligned}\Phi(x_0, y_0) &= \int_{x_a}^{x_b} E^2\, dx \\ &= \int_{x_a}^{x_b} \left[\int_{x_0}^{x} [-\varepsilon_{yy}(x', y_0)]\, dx' \right. \\ &\quad \left. + u(x_0, y_0) - u_m(x, y_0)\right]^2 dx,\end{aligned} \tag{8}$$

where x_a and x_b are the extents of an arbitrary region of interest (ROI). To estimate the lateral displacement at (x_0, y_0) based on this definition, the error function is minimized with respect to $u(x_0, y_0)$. That is,

$$\begin{aligned}u_{LS}(x_0, y_0) = \min_{u(x_0, y_0)} [\Phi(x_0, y_0)] = \frac{1}{x_b - x_a} \int_{x_a}^{x_b} \\ \cdot \left(u_m(x, y_0) - \int_{x_0}^{x} [-\varepsilon_{yy}(x', y_0)]\, dx'\right) dx,\end{aligned} \tag{9}$$

where $u_{LS}(x_0, y_0)$ is the solution to the least squares minimization. Note that the position (x_0, y_0) is independent of the choice of the ROI and that the spatial resolution in the estimated lateral displacement is determined only by the spatial resolution in lateral displacement and normal axial strain measurements and not by the dimension of the ROI.

The least squares error estimate defined in (9) uses both lateral displacements and normal axial strains obtained from speckle tracking. This estimate leads to markedly reduced lateral displacement error if the measured normal axial strain is significantly less noisy than the measured lateral displacement. To understand this, consider a discrete realization of (9) where both lateral and axial displacement images are discretized onto a uniform grid (i.e., $x = n\Delta, y = m\Delta$, where Δ is the grid step size). Choosing the ROI for least squares analysis as a $2M + 1$ lateral window centered at position (n_0, m_0), the discretized approximation to (9) is

$$\begin{aligned}u_{LS}(n_0, m_0) = &\frac{1}{2M+1}\left[\sum_{k=-M}^{M} u_m(n_0 + k, m_0)\right] \\ &- \frac{1}{2M+1}\left[\Delta \sum_{k=-M}^{M} \sum_{n'=0}^{k} -\varepsilon_{yy}(n_0 + n', m_0)\right]\end{aligned} \tag{10}$$

where a simple finite difference approximation has been used for the integrals. Combining terms in the double sum, this expression reduces to

$$\begin{aligned}&u_{LS}(n_0, m_0) \\ &= \frac{1}{2M+1}\left[\sum_{k=-M}^{M} u_m(n_0 + k, m_0)\right] \\ &\quad + \frac{\Delta}{2M+1}\left[M\varepsilon_{yy}(n_0, m_0) + \sum_{k=-M}^{M} (M + 1 - |k|)\right. \\ &\quad \left. \cdot\, \varepsilon_{yy}(n_0 + k, m_0)\right].\end{aligned} \tag{11}$$

The variance in estimated displacements obtained from (11) can be easily determined from a propagation of error analysis. The first term in (11) represents the average displacement over the ROI. To simplify the analysis, assume that the lateral displacement noise in the ROI is additive and white. Then, the variance in the first term of (11) is

$$\sigma_{LS_1}^2 = \frac{\sigma_u^2}{2M+1}, \tag{12}$$

where σ_u^2 is the variance in the measured lateral displacements. Similarly, assuming that in the ROI the strain noise at all points

is additive and white, then the variance in the second term of (11) is

$$\sigma^2_{LS_2} = \frac{(2M^3 + 15M^2 + 13M + 3)}{3(2M+1)^2}\Delta^2\sigma^2_\varepsilon, \qquad (13)$$

where σ^2_ε is the variance in the measured normal axial strain. If the noise processes are not white, which is true in practice, then these terms must be modified to include correlation terms, increasing their value.

If the normal axial strain is computed using a finite difference approximation, the strain variance is simply related to the axial displacement variance

$$\sigma^2_\varepsilon = \frac{2}{\Delta^2}\sigma^2_v, \qquad (14)$$

where σ^2_v is the variance in the axial displacement, again assuming independence. This value will be reduced if the noise process is correlated. Using these expressions, and assuming that the lateral displacement noise and axial strain noise are uncorrelated, the variance in the estimated lateral displacement based on (10) is

$$\begin{aligned}\sigma^2_{LS} &= \sigma^2_{LS_1} + \sigma^2_{LS_2} \\ &= \frac{1}{2M+1}\sigma^2_u + \frac{2(2M^3 + 15M^2 + 13M + 3)}{3(2M+1)^2}\sigma^2_v.\end{aligned} \qquad (15)$$

In the limit that the number of points in the ROI is large (i.e., $M \gg 1$), the total variance can be approximated as

$$\sigma^2_{LS} = \frac{1}{2M+1}\sigma^2_u + \frac{M}{3}\sigma^2_v. \qquad (16)$$

To quantify estimation error reduction with incompressibility processing, the relationship between axial and lateral displacement variance must be known. From the analysis in the Appendix, $\sigma^2_u \approx 40\ (\text{f/num})^2\sigma^2_v$. Rewriting (15) with this assumption yields

$$\begin{aligned}\frac{\sigma^2_{LS}}{\sigma^2_u} &= \frac{1}{2M+1} + \frac{2(2M^3 + 15M^2 + 13M + 3)}{3(2M+1)^2(40\ (\text{f/num})^2)} \\ &\approx \frac{1}{2M+1} + \frac{M}{60\ (\text{f/num})^2} \qquad M \gg 1.\end{aligned} \qquad (17)$$

Reducing the variance in lateral displacement estimates with incompressibility processing improves the SNR of lateral displacement images. The SNR improvement is simply the inverse of (17), i.e., SNR improvement $= \sigma^2_u/\sigma^2_{LS}$. This function is plotted in Fig. 1 for f/nums of 2, 4, and 8, where the ROI width is $2M + 1$. Note that for small values of M, the first term of (17) dominates the potential gain in lateral displacement SNR using incompressibility processing. The influence of the second term can be seen for large M; it is a strong function of the f/num of the system, or alternatively of the strain noise variance.

As an initial test of incompressibility processing's ability to reduce lateral displacement error, a simple 1-D simulation was performed. The discretized lateral displacement was assumed to be 256 points long with Δ equal to 1 mm. Over the first 128 points this function was modeled as a straight line with slope equal to 0.1 mm per pixel, whereas over the second 128 points it was modeled as a straight line with slope equal to 0.25 mm per pixel. The magnitude of the displacement at point 128 was assumed to be 0 mm. For this function, the normal lateral strain was 0.10 over the first 128 points and 0.25 over the second 128 points. Thus, there was a strain discontinuity at the central point.

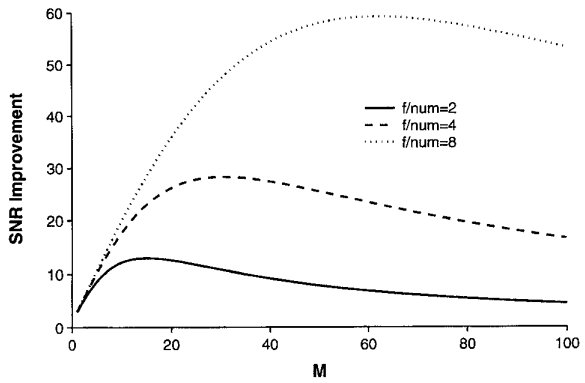

Fig. 1. Theoretical improvement in lateral displacement SNR using incompressibility processing.

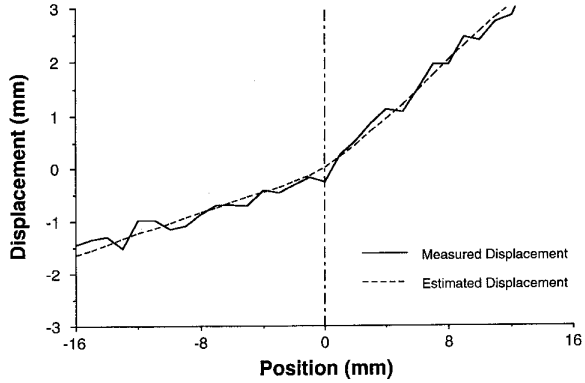

Fig. 2. One-dimensional simulation results comparing measurements and incompressibility processed estimates of the lateral displacement.

A zero-mean uniformly distributed independent random displacement error was added to each of the 256 displacement values. The total function simulates the "measured" displacement that would be obtained from speckle tracking. Similarly, a zero-mean uniformly distributed independent random strain error was added to each of the 256 strain values. The variance in the strain was $\sigma^2_u/(80\Delta^2)$, where σ^2_u is the lateral displacement variance. This error simulates strain noise for an f/num of two (see the Appendix) where the incompressibility condition was used to estimate the normal lateral strain (i.e., the normal lateral strain simply equals the negative of the measured normal axial strain).

In Fig. 2, the "measured" displacement is compared to the displacement estimated from (10), where an ROI of 31 mm (i.e., $M = 15$, near optimal for an f/num of two) was used. These functions are presented over a small region centered at the strain discontinuity. As expected, the estimated displacement is a much smoother function than the measured.

The sharp increase in slope (i.e., strain) is also preserved in the region of the strain discontinuity, even though a large ROI was used. Thus, no spatial resolution is lost with incompressibility processing.

The results presented in Fig. 2 indicate that incompressibility processing can be used to reduce error in lateral displacements estimated by speckle tracking. In the next section, we further test this assertion with experimental studies on tissue equivalent gelatin phantoms.

III. Experimental Methods

Experiments were performed on gelatin-based phantoms using controlled surface deformations. These cylindrical gels were constructed to quantitatively simulate the mechanical and ultrasonic properties of soft tissue. Methods to fabricate them are detailed in previous publications [7], [13]. Two phantoms were used for an initial test of incompressibility processing. One was an 88-mm diameter 140-mm long homogeneous cylindrical phantom of 5.5% by weight gelatin. The other was identical except that a cylindrical hole 32 mm in diameter was made along the longitudinal axis and backfilled with 12% by weight gelatin to simulate a hard inclusion. Ultrasonic scattering centers were created by adding polystyrene microspheres to both gels.

The cylindrical axis of the gel was placed perpendicular to the axis of a 1-D ultrasound transducer array imaging the central plane of the phantom. The 82-mm wide 128-element 3.5-MHz array was attached to the bottom of a water tank, used to ultrasonically couple the array and phantom. The deformation was controlled with vertical displacement of a hydraulically driven piston connected to a 14.2-mm wide rigid rectangular block extending the entire length of the phantom. As reported previously [7], [13], this deformation system closely approximates a plane strain state in the region of the imaging plane. The position of the piston was monitored by the round-trip echo time to it from the two center elements of the array.

Complex demodulated (in-phase and quadrature or I and Q) images were reconstructed and the normal axial strain, ε_{yy}, was computed using the methods of [4] and [13] with a constant f/num of approximately three. The strain computation uses a phase unwrapping technique to properly accumulate the axial strain over a large set of small differential displacements to produce a total strain image referenced to the final position of the phantom. Thus large total displacements and strains can be measured without speckle decorrelation due to strain. For the results presented here, the vertical piston was displaced a total of 6 mm over a set of 20 differential displacements of 0.3 mm each. The 2-D window used in the strain calculations resulted in a spatial resolution of about 2.7 $\times$ 2.7 mm. Additionally, differential axial and lateral displacements were computed using a slight variation on the traditional 2-D correlation technique of [6]. This 2-D technique was modified to operate on the same complex (I and Q) images used in strain calculations, rather than RF or envelope-detected data. Additionally, the 2-D window used for correlation tracking was the same as that used for strain measurements. Both differential lateral and axial displacements were also accumulated properly to produce total displacement images referenced to the final position of the phantom.

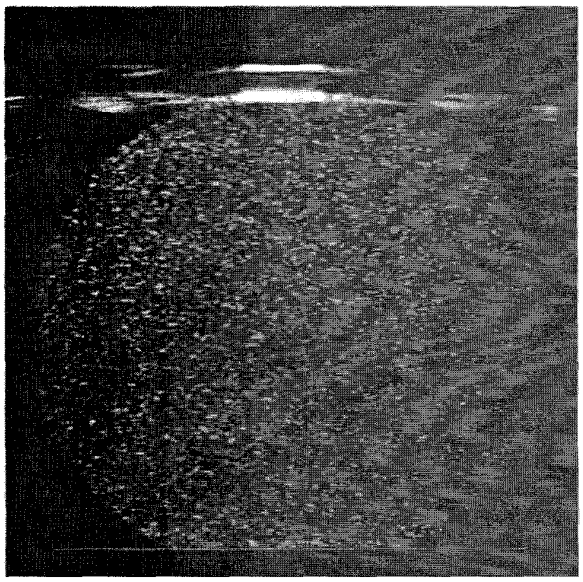

Fig. 3. Conventional B-scan image of one of the gel-based phantoms.

Lateral displacements were also computed using incompressibility processing. Along a given range, the displacement was first estimated at the center pixel of the image employing a finite difference approximation of (9), where a second-order Taylor series expansion approach was used for integration. The 25.2-mm wide ($M = 64, \Delta = 0.195$ mm) ROI was symmetric about this position. The calculation was repeated with a symmetric ROI of the same size, stepping a pixel at a time to the right, until reaching a lateral position where lateral displacements measured from speckle tracking were greatly in error [see Figs. 4(a) and 5(a)]. Large lateral displacement errors are the direct result of imperfect beam forming in our synthetic aperture system at large steering angles. To overcome these imperfections, a finite difference approximation of (6) was used to estimate the displacement for the remaining pixels on this row to the right. The rightmost displacement estimate calculated using (9) was used as the integration constant, $u(x0, y0)$, in (6). A similar process was used for pixels to the left of the image center. The overall process was repeated for all ranges in the image. To test the accuracy of lateral displacement estimates, theoretical displacements within the phantom were computed using a finite difference method reported previously in [7].

IV. Experimental Results

In Fig. 3, a conventional B-scan of the homogeneous phantom is shown in its final position, i.e., after the piston was displaced vertically downward 6 mm. This image, and all subsequent images, are displayed over a 100 $\times$ 100 mm area with the piston located at the top of the image and the transducer at the bottom. The B-scans are not of the best quality, with significant artifacts outside and at the edges

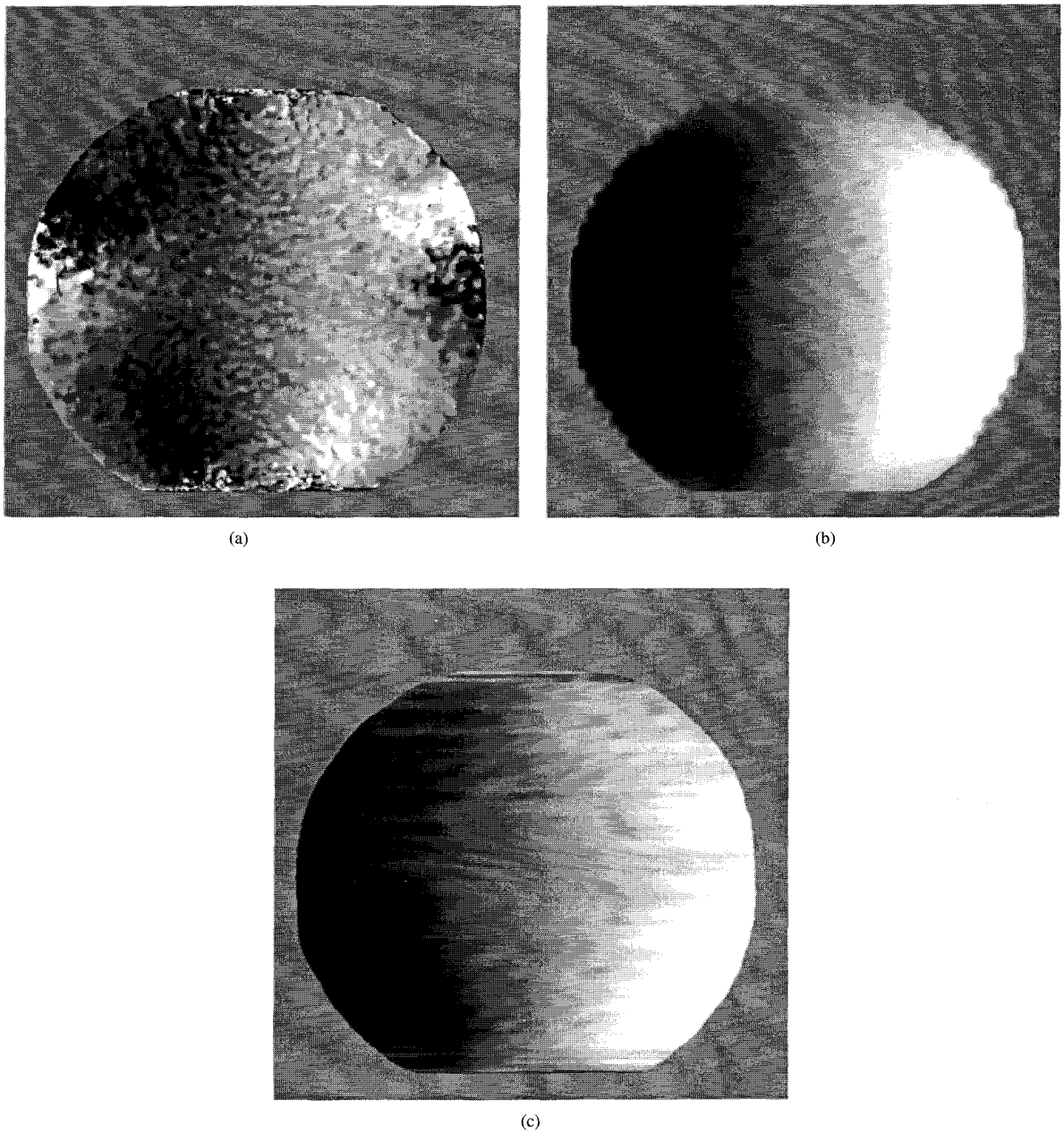

Fig. 4. Lateral displacement images of the homogeneous gel-based phantom displayed over the same dynamic range: (a) traditional 2-D correlation speckle tracking, (b) theoretical, and (c) incompressibility processing.

of the phantom, because synthetic aperture rather than full phased array reconstruction was used. Even so, data are of sufficient quality for accurate axial displacement and strain measurements as described in [13].

Lateral displacements for the homogeneous phantom are shown in Fig. 4. The images are displayed on the same linear gray scale where mid-gray represents no motion, full white motion 1.0 mm to the right, and full black motion 1.0 mm to the left. The displacement measured using traditional 2-D correlation speckle tracking is shown in Fig. 4(a). As noted previously, there are significant artifacts in lateral tracking due to poor synthetic aperture beamforming at the sides of the phantom, corresponding to the maximum steering angle. The theoretical displacement is shown in Fig. 4(b) and the reconstructed displacement using the incompressibility property is shown in Fig. 4(c).

Lateral displacements for the phantom with a single hard inclusion are shown in Fig. 5 using the same quantitative gray scale. Again, the displacement measured with speckle tracking is shown in Fig. 5(a), theoretical results in Fig. 5(b), and the reconstructed displacement in Fig. 5(c). The position of the inclusion is clearly seen in Fig. 5(c).

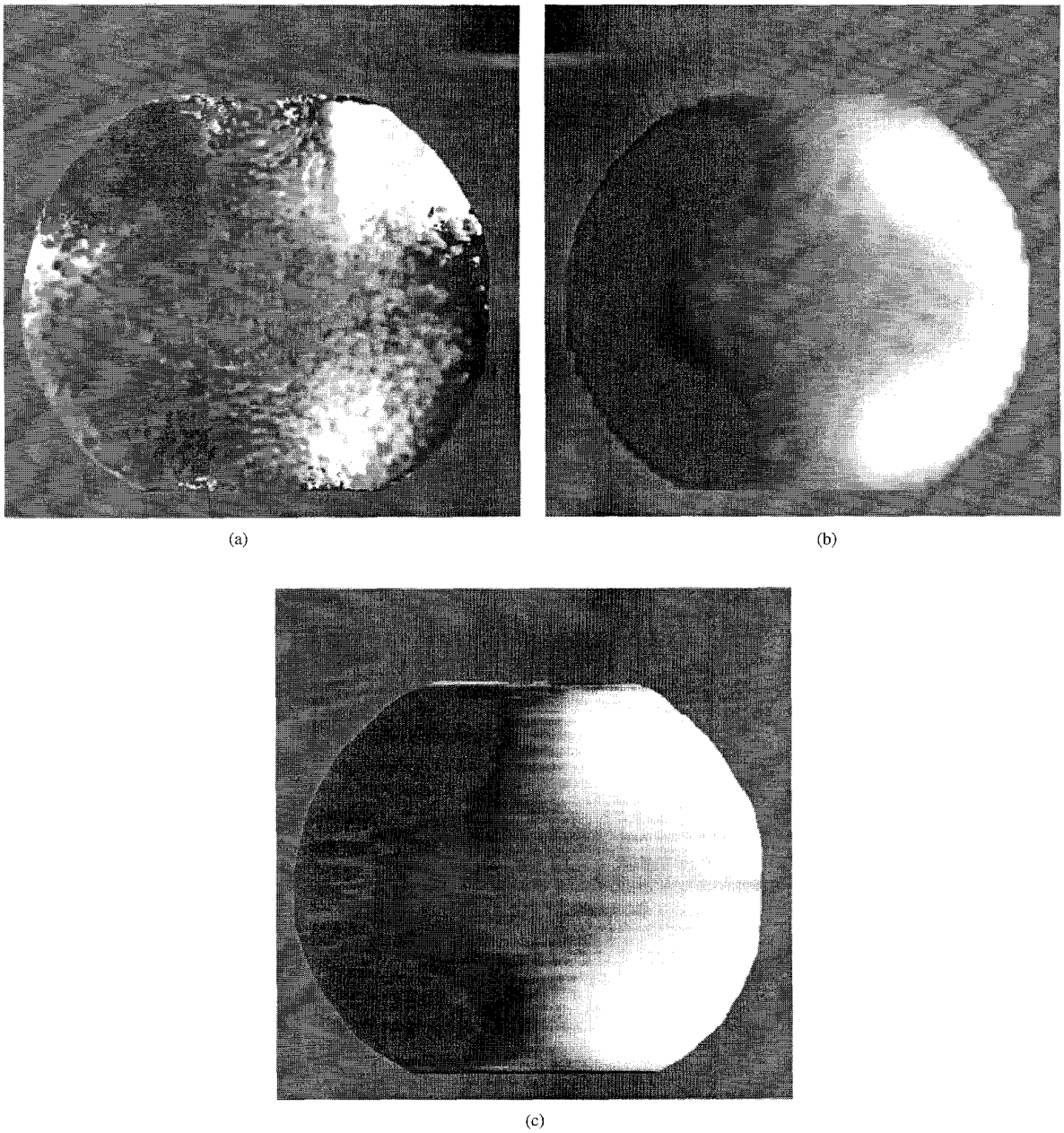

Fig. 5. Lateral displacement images of the gel-based phantom with single hard inclusion displayed over the same dynamic range: (a) traditional 2-D correlation speckle tracking, (b) theoretical, and (c) incompressibility processing.

A more quantitative comparison of these results is presented in Fig. 6. Fig. 6(a) shows the three different lateral displacement estimates along a single range for the homogeneous phantom. The range chosen was a horizontal line passing through the more accurate correlation tracking estimates above the center of the cylindrical phantom. Fig. 6(b) displays the lateral displacement estimated along the same range for the phantom with a hard inclusion.

Variances of lateral displacement estimates using correlation tracking and the incompressibility property were measured for both phantoms. The variance of the lateral displacement was calculated along a 60-mm long vertical line in the center of the phantom. This region had the best correlation tracking estimates and the true displacement along this line should be constant due to symmetry, so that any variance in the displacement should accurately reflect noise in these estimates. Lateral displacements from correlation tracking and incompressibility processing along this line are shown in Fig. 7 for the homogenous phantom. For the homogeneous phantom, the measured ratio of variances, σ_u^2/σ_{LS}^2, was about 11.7. The ratio for the hard inclusion phantom was larger, about 16.0.

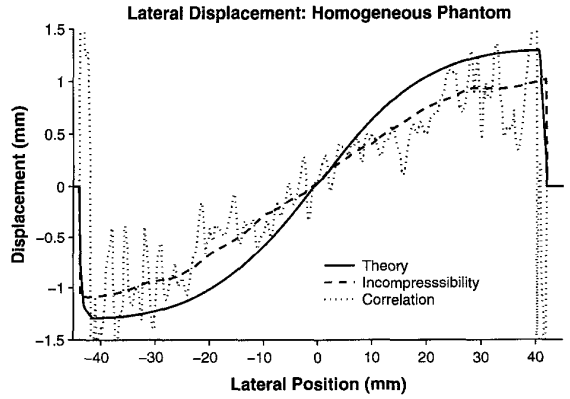

(a)

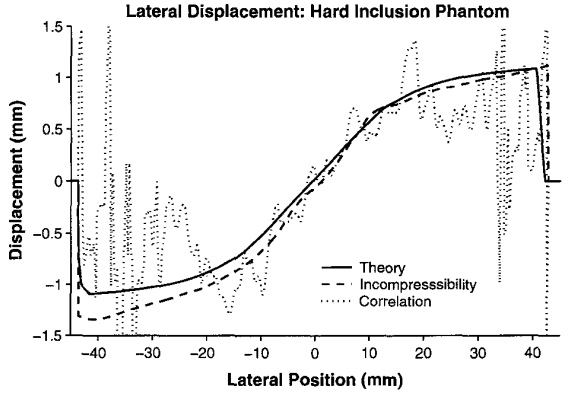

(b)

Fig. 6. Horizontal lateral displacement A-scans: (a) homogeneous phantom, and (b) phantom with single hard inclusion.

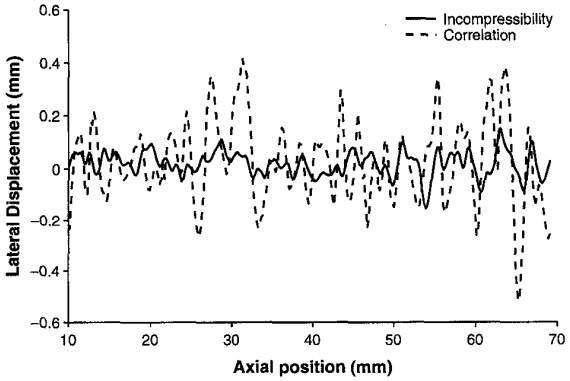

Fig. 7. Vertical lateral displacement A-scan for the homogeneous phantom.

V. Discussion

Comparison of the lateral displacement images in Figs. 4 and 5 clearly shows that incompressibility processing significantly improves the SNR over traditional correlation tracking. This was quantitatively confirmed by SNR measurements. The expected SNR improvement is difficult to estimate due to the effects of correlation in the measured data which, for simplicity, are not included in the discussion above. However, SNR improvements can be estimated using data separated by the autocorrelation half width ($R_{1/2}$), representing approximately independent values. Defining an effective ROI half width, $M_{\text{eff}} = M/R_{1/2}$, (17) can be evaluated simply by replacing M with M_{eff}. For both phantoms, the autocorrelation half width was about 15 pixels ($\approx$3 mm), resulting in an M_{eff} of about 4.3. Since the system used a constant f/num of three for reconstruction, the expected SNR improvement should be about nine. Measured SNR improvements were larger, about 11.7 and 16.0 for the two phantoms.

Differences between theoretical and incompressibility processed displacements seen in Fig. 6 may be caused by inexact modeling of experimental conditions, e.g., phantom and inclusion position and the relative Young's modulus of the inclusion, or underestimation of the lateral displacement by correlation speckle tracking. Nevertheless, these plots along with Fig. 7 clearly show that incompressibility processing can greatly improve lateral displacements estimated by correlation tracking.

Variations on the basic algorithms used for incompressibility processing will be explored. The least-squares estimate presented here was based on a 1-D error term. Estimator performance may improve if the algorithm is expanded to two dimensions. Additionally, a weighted least-squares estimate, where the weighting is a function of the correlation coefficient from speckle tracking, will be explored. Such weighting may significantly reduce the effects of inaccurate or high-variance displacement estimates.

In general, to fully characterize deformations of an elastic object, the complete strain tensor must be computed. For an incompressible material in a plane strain state, the normal axial strain and the shear strain are the only independent nonzero components. The shear strain is defined as

$$\varepsilon_{xy}(x,y) \equiv \varepsilon_{yx}(x,y) = \frac{1}{2}\left(\left.\frac{\partial u}{\partial y}\right|_{(x,y)} + \left.\frac{\partial v}{\partial x}\right|_{(x,y)} \right). \quad (18)$$

The axial term, $\partial v/\partial x$, in the unknown shear strain can be estimated with high precision using phase sensitive tracking techniques. Estimates of the lateral term, $\partial u/\partial y$, computed from spatial derivatives of noisy tracking measurements should improve with displacements estimated by incompressibility processing. In future studies, we will examine methods similar to those presented in this paper to further reduce error by directly estimating the lateral term in the shear strain component.

Finally, it has not escaped our attention that these same methods may be applied to color flow images. With slight modification, it may be possible to accurately estimate flow orthogonal to the ultrasound beam direction using incompressibility processing, if out-of-plane flow gradients are small.

Appendix

Displacement variance can be approximated from an analysis of correlation errors [14]. Assuming that measurement noise is additive and white and has a small magnitude with respect to the signal, and that the powers of the two signals

being correlated are the same, the variance of the fluctuation of the peak position of the cross-correlation function ξ can be shown to be [15], [16]

$$\sigma_\xi^2 = \frac{4\pi}{W}\frac{1}{\mathrm{SNR}}, \tag{19}$$

where W is the normalized second moment of the signal power spectrum

$$W = \frac{\int \omega^2 |G(\omega)|^2 \, d\omega}{\int |G(\omega)|^2 \, d\omega}. \tag{20}$$

Although simplistic since it ignores decorrelation effects, this model can give reasonable estimates of the relative variance of displacement estimates if the correlation coefficient is close to one.

To compute W in the axial direction, assume that the pulse has a Gaussian envelope so that it has a Gaussian power spectrum

$$|G_{\mathrm{time}}(\omega)|^2 = G_0 e^{-(1/2)((\omega-\omega_0)/\sigma_\omega)^2}. \tag{21}$$

Using the properties of a normalized Gaussian function, the pulse power and the second moment of the power spectrum are easily determined to be

$$\int |G_{\mathrm{time}}(\omega)|^2 \, d\omega = G_0 \sigma_\omega \sqrt{2\pi}, \tag{22}$$

$$\int \omega^2 |G_{\mathrm{time}}(\omega)|^2 \, d\omega = G_0 \sigma_\omega \sqrt{2\pi}(\omega_0^2 + \sigma_\omega^2). \tag{23}$$

Consequently, the normalized second moment of the power spectrum in the axial direction is simply

$$W_{\mathrm{time}} = (\omega_0^2 + \sigma_\omega^2). \tag{24}$$

If we assume that the fractional bandwidth, denoted BW, is defined as the full width half maximum power bandwidth of the Gaussian power spectrum, then the variance of the Gaussian can be rewritten as

$$\sigma_\omega^2 = \frac{(BW\omega_0)^2}{8\ln(2)}. \tag{25}$$

Equation (24) then becomes

$$W_{\mathrm{time}} = \omega_0^2\left(1 + \frac{BW^2}{8\ln(2)}\right). \tag{26}$$

To analyze the variance of ξ as a function of space rather than time, as shown above, the spatial power spectrum must be computed. Using the identity

$$z = \frac{1}{2}ct \Rightarrow \omega_z = \omega_t\frac{2}{c} \Rightarrow \omega_{z0} = \omega_0\frac{2}{c} = \frac{4\pi}{\lambda}, \tag{27}$$

where z is the axial distance, c is the sound velocity, and λ is the wavelength, the normalized axial second moment of the spatial power spectrum is

$$W_{\mathrm{axial}} = \left(\frac{4\pi}{\lambda}\right)^2\left(1 + \frac{BW^2}{8\ln(2)}\right). \tag{28}$$

To compute W laterally, assume continuous wave excitation of a linear array of length L with no aperture apodization. Then, the receive directivity function is the Fourier transform of the aperture function

$$D_R(\sin(\theta)) = D_0\frac{\sin\left(\pi L\frac{\sin(\theta)}{\lambda}\right)}{\pi L\frac{\sin(\theta)}{\lambda}}, \tag{29}$$

where θ is the angle from the array normal. Equation (29) can be rewritten in terms of the lateral distance x using the identity $\sin(\theta) = x/R$, where R is the range. If the system uses a constant f/num (f/num $= R/L$), then (29) becomes

$$D_R(x) = D_0\frac{\sin\left(\frac{\pi x}{\lambda\,\mathrm{f/num}}\right)}{\frac{\pi x}{\lambda\,\mathrm{f/num}}}. \tag{30}$$

Defining the lateral spatial frequency as ω_x, the lateral receive directivity as a function of spatial frequency is simply the Fourier transform

$$D_R(\omega_x) = \begin{cases} D_0\lambda\,\mathrm{f/num}, & |\omega_x| < \dfrac{\pi}{\lambda\,\mathrm{f/num}} \\ 0, & |\omega_x| > \dfrac{\pi}{\lambda\,\mathrm{f/num.}} \end{cases} \tag{31}$$

For the best possible resolution, assume that the system is dynamically focused on both transmit and receive so that the transmit and receive directivity functions are identical. Then, the transmit-receive directivity in the frequency domain becomes the convolution of the transmit and receive directivities

$$D_{TR}(\omega_x) = 2\pi D_0^2\lambda\,\mathrm{f/num}\begin{cases} 1 - \dfrac{\omega_x}{\omega_{xc}}, & 0 < \omega_x < \omega_{xc} \\ 1 + \dfrac{\omega_x}{\omega_{xc}}, & -\omega_{xc} < \omega_x < 0, \\ 0, & |\omega| \geq \omega_{xc} \end{cases} \tag{32}$$

where $\omega_{xc} = 2\pi/\lambda\,\mathrm{f/num}$ is the cutoff spatial frequency. Consequently, the power spectrum of the lateral diffraction pattern is

$$|D_{TR}(\omega_x)|^2 = (2\pi D_0^2\lambda\,\mathrm{f/num})^2 \cdot \begin{cases} \left(1 - \dfrac{\omega_x}{\omega_{xc}}\right)^2, & 0 < \omega_x < \omega_{xc} \\ \left(1 + \dfrac{\omega_x}{\omega_{xc}}\right)^2, & -\omega_{xc} < \omega_x < 0. \\ 0, & |\omega_x| \geq \omega_{xc} \end{cases} \tag{33}$$

From (33), the total power and the second moment of the lateral power spectrum can be computed

$$\int |D_{TR}(\omega_x)|^2 \, d\omega_x = \tfrac{2}{3}\omega_{xc}(2\pi D_0^2\lambda\,\mathrm{f/num})^2, \tag{34}$$

$$\int \omega_x^2 |D_{TR}(\omega_x)|^2 \, d\omega_x = \tfrac{1}{15}\omega_{xc}^3(2\pi D_0^2\lambda\,\mathrm{f/num})^2. \tag{35}$$

So the normalized second moment of the lateral power spectrum is

$$W_{\mathrm{lateral}} = \frac{1}{10}\left(\frac{2\pi}{\lambda\,\mathrm{f/num}}\right)^2. \tag{36}$$

The relative variance of lateral to axial displacement estimates is simply the ratio of their respective variances

$$\frac{(\sigma_\xi^2)_{\text{lateral}}}{(\sigma_\xi^2)_{\text{axial}}} = \frac{\dfrac{4\pi}{W_{\text{lateral}}}\dfrac{1}{\text{SNR}_{\text{lateral}}}}{\dfrac{4\pi}{W_{\text{axial}}}\dfrac{1}{\text{SNR}_{\text{axial}}}} = \frac{W_{\text{axial}}}{W_{\text{lateral}}}\frac{\text{SNR}_{\text{axial}}}{\text{SNR}_{\text{lateral}}}. \tag{37}$$

Assuming that the SNR's are the same in both dimensions, the relative variances become

$$\frac{(\sigma_\xi^2)_{\text{lateral}}}{(\sigma_\xi^2)_{\text{axial}}} = 40(\text{f/num})^2\left[1 + \frac{BW^2}{8\ln(2)}\right]. \tag{38}$$

For a 40% fractional bandwidth system, the term in brackets is only 1.03. By approximating this as one, the estimate of the relative variance for lateral to axial displacements using correlation techniques is

$$\frac{(\sigma_\xi^2)_{\text{lateral}}}{(\sigma_\xi^2)_{\text{axial}}} \approx 40(\text{f/num})^2. \tag{39}$$

ACKNOWLEDGMENT

The authors would like to thank Acuson for supplying the transducer array.

REFERENCES

[1] G. E. Mailloux, A. Bleau, M. Bertrand, and R. Petitclerc, "Computer analysis of heart motion from two-dimensional echocardiograms," *IEEE Trans. Biomed. Eng.*, vol. BME-34, pp. 356–364, May 1987.

[2] I. Akiyama, A. Hayama, and M. Nakajima, "Movement analysis of soft tissues by speckle patterns' fluctuations," in *JSUM Proc.*, Oct. 1986, pp. 615–616.

[3] G. E. Trahey, J. W. Allison, and O. T. V. Ramm, "Angle independent ultrasonic detection of blood flow," *IEEE Trans. Biomed. Eng.*, vol. BME-34, pp. 965–967, Dec. 1987.

[4] M. O'Donnell, A. R. Skovoroda, and B. M. Shapo, "Measurement of arterial wall motion using Fourier based speckle tracking algorithms," in *Proc. 1991 IEEE Ultrason. Symp.*, pp. 1101–1104.

[5] I. A. Hein and W. D. O'Brien, "Current time-domain methods for assessing tissue motion by analysis from reflected echoes—A review," *IEEE Trans. Ultrason., Ferroelect., Freq. Contr.*, vol. 40, pp. 84–102, Mar. 1993.

[6] L. N. Bohs and G. E. Trahey, "A novel method for angle independent imaging of blood flow and tissue motion," *IEEE Trans. Biomed. Eng.*, vol. 38, pp. 290–286, Mar. 1991.

[7] A. R. Skovoroda, S. Y. Emelianov, M. A. Lubinski, A. P. Sarvazyan, and M. O'Donnell, "Theoretical analysis and verification of ultrasound displacement and strain imaging," *IEEE Trans. Ultrason., Ferroelect., Freq. Contr.*, vol. 41, pp. 302–313, May 1994.

[8] Y. C. Fung, *Biomechanics—Mechanical Properties of Living Tissues*. New York: Springer-Verlag, 1981.

[9] A. P. Sarvazyan, "Low frequency acoustic characteristics of biological tissues," *Mech. Polymers*, vol. 4, pp. 691–695, 1975.

[10] L. D. Landau and E. M. Lifshitz, *Theory of Elasticity*. Moscow: Nauka, 1965.

[11] A. R. Skovoroda, S. Y. Emelianov, and M. O'Donnell, "Tissue elasticity reconstruction based on ultrasonic displacement and strain images," *IEEE Trans. Ultrason., Ferroelect., Freq. Contr.*, vol. 42, pp. 747–765, July 1995.

[12] S. Timeshenko and J. N. Goodier, *Theory of Elasticity*. New York: McGraw-Hill, 1951.

[13] M. O'Donnell, A. R. Skovoroda, B. M. Shapo, and S. Y. Emelianov, "Internal displacement and strain imaging using ultrasonic speckle tracking," *IEEE Trans. Ultrason., Ferroelect., Freq. Contr.*, vol. 41, pp. 314–325, May 1994.

[14] E. Weinstein and A. J. Weiss, "Fundamental limitations in passive time-delay estimation—Part II: Wide-band systems," *IEEE Trans. Acoust., Speech, Signal Processing*, vol. ASSP-32, pp. 1064–1077, Oct. 1984.

[15] P. M. Embree, "The accurate measurement of the volume flow of blood by time domain correlation," Ph.D. dissertation, Univ. Illinois, Urbana-Champaign, 1986.

[16] D. L. Liu and M. Saito, "Restoring a δ-pulse train by spectral fitting," *IEEE Trans. Signal Processing*, vol. 40, pp. 2616–2619, 1992.

Mark A. Lubinski (S'94) received the B.S. degree in electrical engineering (with biomedical engineering option), in 1990 from Carnegie-Mellon University, Pittsburgh, PA, and M.S. degrees in bioengineering and electrical engineering (systems), in 1993 and 1994, respectively, from the University of Michigan, Ann Arbor. He is currently pursuing the PhD. in bioengineering, and researching ultrasonic elasticity imaging.

Before beginning his graduate work, he worked as a Computer Engineer in the Department of Neurophysiology at Children's Hospital of Pittsburgh. While at the University of Michigan he was a National Science Foundation Graduate Fellow in Bioengineering and a GAANN Fellow. He is currently a Graduate Student Research Assistant at the University of Michigan, working in the Biomedical Ultrasonics Laboratory. His research interests include signal processing, medical imaging, and motion estimation.

Mr. Lubinski is a member of Tau Beta Pi and Eta Kappa Nu.

Stanislav Y. Emelianov (M'93) was born in May 1966. He received the B.S. and M.S. degrees in physics, in 1986 and 1989, respectively, from Moscow State University, and the Ph.D. degree in physics, in 1993, from Moscow State University and the Institute of Mathematical Problems of Biology of the Russian Academy of Sciences, Russia.

In 1989, he joined the Institute of Mathematical Problems of Biology, where he was engaged in both mathematical modeling of soft tissue biomechanics and experimental studies of noninvasive methods in medical diagnostics based on tissue elasticity variations. Following his graduate work, he moved to the University of Michigan, Ann Arbor, as a Postdoctoral Fellow in the Electrical Engineering and Computer Science Department working on applications of imaging systems for medical diagnosis and nondestructive testing. He is currently a Research Associate at the Biomedical Ultrasonics Laboratory at the University of Michigan and involved primarily in the theoretical and practical aspects of ultrasound elasticity imaging. He is the author of several scientific papers. His research interests are in the areas of tissue biomechanics, medical imaging systems, and nondestructive material testing.

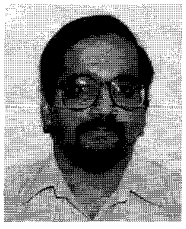

K. R. Raghavan (S'90–M'95) received the B.Tech. degree in electrical engineering from the Indian Institute of Technology, Bombay, in 1987, and the M.S. and Ph.D. degrees in electrical engineering from Villanova University, Villanova, PA, in 1988, and the University of Michigan, Ann Arbor, in 1994, respectively.

He is currently Director of Engineering at Triada, Limited, where he is working on developing and applying novel algorithms for data mining, data compression, and pattern recognition problems.

Dr. Raghavan is a member of Eta Kappa Nu and Sigma Xi.

Andrew E. Yagle (M'85) was born in Ann Arbor, MI, in 1956. He received the B.S.E. and B.S.E.E. degrees from the University of Michigan, Ann Arbor, in 1977 and 1978, respectively, and the S.M., E.E., and Ph.D. degrees from M.I.T., Cambridge, MA, in 1981, 1982, and 1985, respectively.

While at M.I.T., he received an Exxon Teaching Fellowship from 1982 to 1985. Since September 1985 he has been with the Department of Electrical Engineering and Computer Science of the University of Michigan, Ann Arbor, where he is currently an Associate Professor. His research interests include fast algorithms for digital signal processing, multiresolution and iterative algorithms in medical imaging, multidimensional inverse scattering, phase retrieval, and linear least-squares estimation.

Dr. Yagle received the NSF Presidential Young Investigator Award in 1988 and the ONR Young Investigator Award in 1990. He received H. H. Rackham School of Graduate Studies Research Partnership Awards in 1990 and 1993. He has received several teaching awards, including the College of Engineering Teaching Excellence Award in 1992, the Eta Kappa Nu Professor of the Year Award in 1990, and the Class of 1938e Distinguished Service Award in 1989. He is currently an Associate Editor of the IEEE TRANSACTIONS ON IMAGE PROCESSING, IEEE SIGNAL PROCESSING LETTERS, and *Multidimensional Systems and Signal Processing*. He is also a member of the Digital Signal Processing Technical Committee, a past Associate Editor of the IEEE TRANSACTIONS ON SIGNAL PROCESSING, and Co-technical Chair of ICASSP-95, in Detroit, MI.

Andrei R. Skovoroda, for photograph and biography, see this issue, p. 246.

Matthew O'Donnell (M'79–SM'84–F'93), for photograph and biography, see p. 14 of the January 1996 issue of this TRANSACTIONS.